Scientia Iranica (2025) **32**(1): 6623

Sharif University of Technology

Scientia Iranica

Transactions on Computer Science & Engineering and Electrical Engineering

https://scientiairanica.sharif.edu

Flux-weakening control of linear induction motor drives considering the primary resistance and end effect

Pegah Hamedani *

Department of Railway Engineering and Transportation Planning, University of Isfahan, Isfahan, Iran.

* Corresponding author: p.hamedani@eng.ui.ac.ir (P. Hamedani.)

Received 10 April 2022; received in revised form 17 August 2022; accepted 7 November 2022

Keywords

End effect;

Flux-weakening control;

Fuzzy logic control;

Linear induction motor drive;

Voltage constraint;

Current constraint.

Abstract

Indirect Field-Oriented Control (IFOC) of a Linear Induction Motor (LIM) drive is an important challenge because of the end effect and nonlinear behavior of the LIM drive. It becomes more complex in high-speed applications and Flux-Weakening (FW) regions when current and voltage constraints must be satisfied. Moreover, considering the primary resistance in voltage constraint inequality makes the calculations even more complicated. This work presents a new FW control algorithm for LIM drives, considering the end effect and the primary resistance. Consequently, the reference d-axis current and maximum q-axis current are modified considering the primary resistance and end effect. Accordingly, new control strategies for the partial and full FW regions are implemented in a LIM drive. Fuzzy Logic Controller (FLC) has been used to overcome the nonlinear behavior of LIM drive and achieve appropriate dynamic characteristics. Simulation results validate the effectiveness of the suggested LIM drive based on FLC in different speed regions. Moreover, results manifest that in a LIM drive with end effect consideration, the base and the critical speeds are not constant. As the LIM speed increases, the base frequency reduces, whereas the critical frequency increases.

1. Introduction

Linear Induction Motors (LIMs) are a special type of induction motor that can directly generate linear force and motion. Therefore, they can be used in applications that require linear motion, such as electric trains [1]. In addition, these motors have all the advantages of rotary induction motors such as low maintenance, low cost, simple and strong structure, and high starting force.

All methods of controlling rotary induction motor drives such as scalar control, direct torque control, Indirect Field-Oriented Control (IFOC), and model predictive control can also be used for LIMs [2-4]. But the control of LIMs is more complicated due to the end effect [5-9]. The most appealing strategy to control LIMs is the IFOC method. Using the IFOC concept, the thrust and the flux components must be decoupled and separately controlled [8-10]. In this strategy, the *q*-axis secondary flux is set to zero and the *d*-axis secondary flux is considered constant and equal to its nominal value. IFOC of the LIM drive presents a perfect speed control performance.

But the important issue is choosing a suitable model to control the LIM drive, which takes into account the end effect and is also simple and practical. A famous per-phase equivalent model for the LIM considering the end effect was introduced by Duncan [11]. Accordingly, the dynamic model of a LIM for electric drive applications has been developed [12].

On the other hand, traction drive applications such as high-speed electric trains usually need wide-range speed control. For these applications, Flux-Weakening (FW) speed control strategy is required to deliver constant power at higher speeds [13-20]. In addition, when the speed raises, the produced torque and power of the motor are limited due to the rated voltage and current values of the inverter, which supplies the electric motor drive [2]. As a result, in a perfectly performed FW control strategy, the machine flux must be suitably weakened, and simultaneously, the voltage and current limits should be satisfied [18-19]. In the traditional FW strategy, as the motor speed increases, the rotor flux decreases inversely proportional to the speed. However, in the conventional methods, the voltage constraint may not be satisfied. Therefore, the maximum

To cite this article:
P. Hamdani "Flux-weakening control of linear induction motor drives considering the primary resistance and end effect", *Scientia Iranica* (2025), **32**(1): 6623. https://doi.org/10.24200/sci.2022.60081.6623

torque and proper dynamic control of the motor drive is provided. To overcome this issue and to obtain higher torque values, improve the dynamic response, and satisfy the current and voltage constraints in the whole FW area, the modified IFOC control strategy has been proposed in the FW area [18-20].

So far, most of the researches related to the FW control of electric motor drives have been in the field of rotating induction motors [21-31]. In [32,33], only Maximum Torque Per Ampere (MPTA) control strategy has been used for control of LIM drive and partial FW and full FW strategies are not utilized. Furthermore, only the experimental results of an arc induction machine are represented. Therefore, comparing the results of the present work with these works doesn't make sense. In [34], the FW control strategy has been modified for LIMs considering the end effect. But, the impact of primary resistance has been neglected in calculations.

Due to the issues discussed above, the principal purpose of this work is to concentrate more accurately on the FW control of LIMs regarding the end effect. In this work, the primary resistance has been considered in calculating the FW equations. The main contributions of this research are as follows:

- To provide a new FW control pattern for the LIM drive considering the end effect and primary resistance;
- To extract the reference *d*-axis current and the reference maximum *q*-axis current in three operational speed regions regarding the end effect and the primary resistance;
- To calculate the base and the critical speeds during the running time of the algorithm considering the end effect and primary resistance;
- Implementation of Fuzzy Logic Controller (FLC) to overcome the nonlinear behavior and to improve the dynamic characteristics of the LIM drive in FW region.

The structure of this paper is as follows; In Section 2, the dynamic model of the LIM is presented. The IFOC scheme of the LIM drive is explained in Section 3. Then in Section 4, the current and voltage constraints are discussed considering the primary resistance. Sections 5 and 6 explain the FW control strategy and the overall control diagram, respectively. In Section 7, the FLC is represented. Section 8 provides the simulation results of a LIM drive with FW speed control considering the primary resistance. Conclusions are given in Section 9.

2. LIM drives model

The voltage and flux equations of the three-phase LIM considering the end effect can be written as follows [35]:
Primary voltage equations:

$$\begin{aligned} v_{qs} &= R_s i_{qs} + \omega\lambda_{ds} + p\lambda_{qs}, \\ v_{ds} &= R_s i_{ds} - \omega\lambda_{qs} + p\lambda_{ds}. \end{aligned} \tag{1}$$

Secondary voltage equations:

$$\begin{aligned} v_{qr} &= R'_r i_{qr} + (\omega - \omega_r)\lambda_{dr} + p\lambda_{qr} = 0, \\ v_{dr} &= R'_r i_{dr} - (\omega - \omega_r)\lambda_{qr} + p\lambda_{dr} = 0. \end{aligned} \tag{2}$$

Primary flux linkage equations:

$$\begin{aligned} \lambda_{qs} &= L_{ls} i_{qs} + L_m\{1 - f(Q)\}(i_{qs} + i_{qr}), \\ \lambda_{ds} &= L_{ls} i_{ds} + L_m\{1 - f(Q)\}(i_{ds} + i_{dr}). \end{aligned} \tag{3}$$

Secondary flux linkage equations:

$$\begin{aligned} \lambda_{qr} &= L'_{lr} i_{qr} + L_m\{1 - f(Q)\}(i_{qs} + i_{qr}), \\ \lambda_{dr} &= L'_{lr} i_{dr} + L_m\{1 - f(Q)\}(i_{ds} + i_{dr}). \end{aligned} \tag{4}$$

In which the magnetizing inductance is defined as:

$$L_m \cong L_{m_0}(1 - f(Q)),$$

where,

$$f(Q) = \frac{(1 - e^{-Q})}{Q}, \qquad Q \cong \frac{D\,R'_r}{L'_r\,v_r}. \tag{5}$$

L_{m_0} is the magnetizing inductance at zero speed. D and v_r are the LIM length and speed, respectively. L'_r and R'_r correspond to the secondary self-inductance and the secondary resistance, respectively [35]. ω_r denotes the secondary angular speed, and ω-ω_r is the slip frequency ($\omega - \omega_r \equiv \omega_{sl}$). The LIM force can be determined as follows:

$$F = \frac{3}{2}\frac{\pi}{\tau}\left(\lambda_{qr} i_{dr} - \lambda_{dr} i_{qr}\right), \tag{6}$$

where τ denotes the motor pole pitch.

3. IFOC method of the LIM drive

According to the IFOC theory in the LIM drives, the secondary flux is aligned with the *d*-axis. Subsequently [36]:

$$\lambda_{qr} = 0, \qquad \frac{d\lambda_{qr}}{dt} = 0. \tag{7}$$

After simplifying and considering the steady-state condition the stator flux equations can be written as [36]:

$$\lambda_{qs} = \left[L_{ls} + \frac{L'_{lr}(1 - f(Q))}{\frac{L'_{lr}}{L_m} + (1 - f(Q))}\right] \times i_{qs}, \tag{8}$$

$$\lambda_{ds} = \left[L_{ls} + L_m(1 - f(Q))\right] \times i_{ds}. \tag{9}$$

The slip frequency ($\omega_{sl} \equiv \omega_e - \omega_r$) is be calculated as:

$$\omega_{sl} = \left[\frac{R'_r}{L'_{lr} + L_m(1 - f(Q))}\right] \times \frac{i_{qs}}{i_{ds}}. \tag{10}$$

The motor thrust can be derived and written as:

$$F = \frac{3}{2}\frac{\pi}{\tau} G(f(Q)) \times i_{ds} i_{qs}, \tag{11}$$

where,

$$G(f(Q)) = \frac{L_m{}^2 . (1 - f(Q))^2}{L'_{lr} + L_m(1 - f(Q))}. \tag{12}$$

4. Current and voltage limits

In practice, the current and voltage constraints imposed from the inverter restrict the operation of an electrical machine drive [34]:

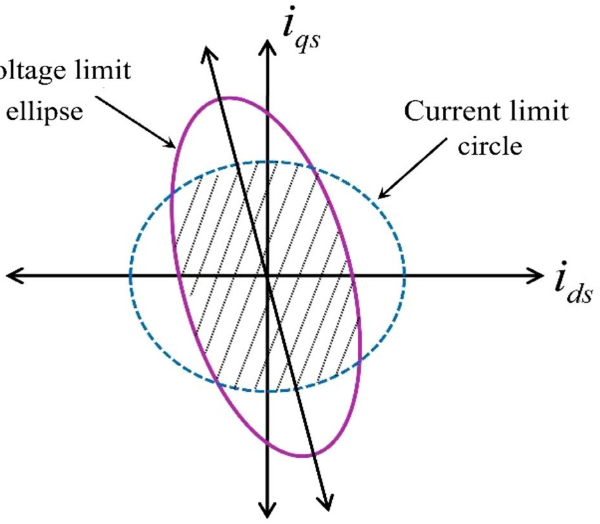

Figure 1. The current and voltage limit curves.

$$(i_{qs})^2 + (i_{ds})^2 \leq I_{max}^2, \tag{13}$$

$$(v_{qs})^2 + (v_{ds})^2 \leq V_{max}^2, \tag{14}$$

where $I_{\max}$ and $V_{\max}$ are the maximum current and voltage values, respectively.

For a LIM drive with the IFOC method in synchronous reference frame, the q and d axis voltages can be calculated as follows [34]:

$$v_{qs} = R_s\, i_{qs} + \omega_e\, K_1\, i_{ds}, \tag{15}$$

$$v_{ds} = R_s\, i_{ds} - \omega_e\, K_2\, i_{qs}, \tag{16}$$

where

$$K_1 = L_{ls} + L_m(1 - f(Q)) = L_s,$$
$$K_2 = L_{ls} + \frac{L'_{lr}(1-f(Q))}{\frac{L'_{lr}}{L_m}+(1-f(Q))} = \sigma L_s,$$
$$\sigma = 1 - \frac{{L_m}^2(1-f(Q))^2}{L_s+L'_r}, \tag{17}$$

where σ denotes the leakage factor.

Substituting Eqs. (15) and (16) into Eq. (14), results in:

$$(R_s\, i_{qs} + \omega_e\, K_1\, i_{ds})^2 + (R_s\, i_{ds} - \omega_e\, K_2\, i_{qs})^2 \leq V_{smax}^2. \tag{18}$$

Figure 1 depicts the current and voltage limits. The feasible operation area is inside the current constraint circle and voltage constraint ellipse. Note that the voltage constraint ellipse shrinks toward the origin as the speed increases.

5. FW control strategy of the LIM

The overall operating range of a three-phase LIM drive can be divided into different areas [18]:

- Constant force area
- FW area
    - Partial FW area
    - Full FW area

The constant force area is related to the operating frequencies below the base frequency, ω_b. The partial FW area is in accordance with the frequencies between the base frequency and the critical frequency, ω_c. Above the critical frequency is the full FW area. Figure 2 demonstrates the operating areas of the LIM drive.

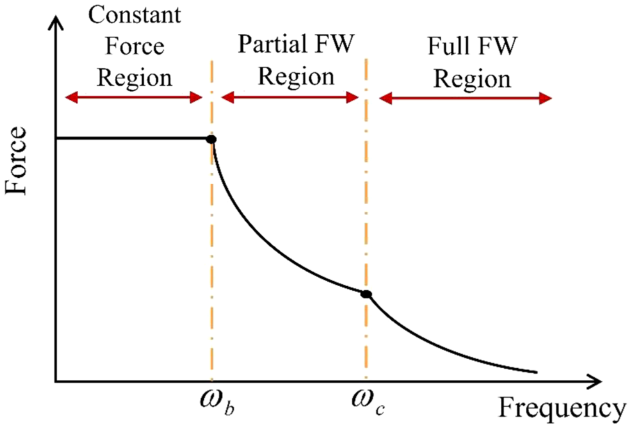

Figure 2. The operating speed areas in the LIM drive.

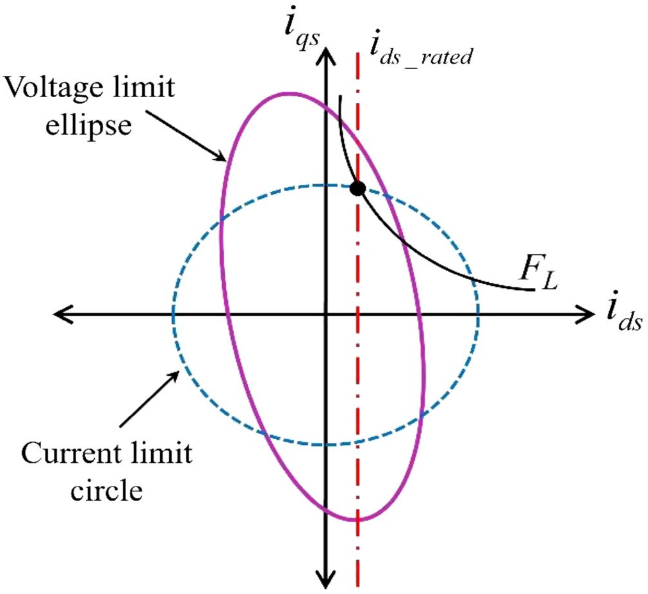

Figure 3. Constant force area.

5.1. Constant force area ($\omega_e < \omega_b$)

In In this area, only the current limit restricts the LIM operation. As represented in Figure 3, in this area, the nominal d-axis current, i_{ds_rated}, might be lower than the d-axis current required for obtaining the maximum force, which is in accordance with crossing point of the ellipse and the circle. To compensate the end effect and to achieve the constant maximum value of the thrust in this area, the command d-axis current, i_{ds}^*, can be derived as [34]:

$$i_{ds}^* = \sqrt{\frac{I_{smax}^2 - \sqrt{I_{smax}^4 - \frac{4\,\alpha^2}{G^2(f(Q))}}}{2}}. \tag{19}$$

The maximum command q-axis current, $i_{qs_{lim}}^*$, can be expressed as follows [34]:

$$i_{qs_{lim}}^* = \sqrt{\frac{I_{smax}^2 + \sqrt{I_{smax}^4 - \frac{4\,\alpha^4}{G^2(f(Q))}}}{2}}, \tag{20}$$

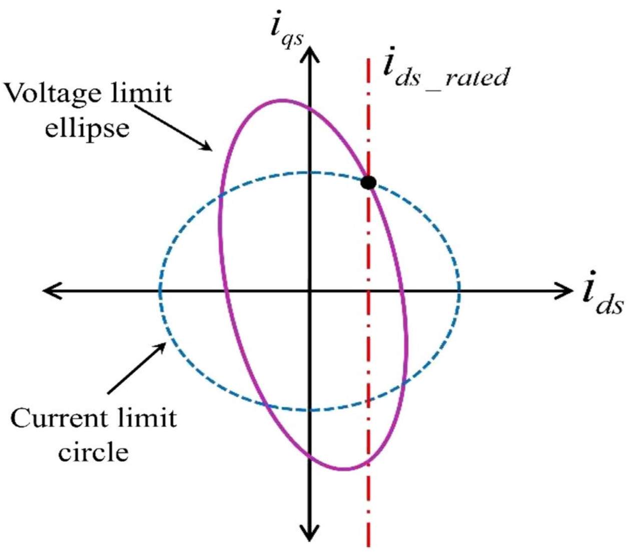

Figure 4. Determination of the base frequency.

where $G(f(Q))$ is defined in Eq. (12).

Moreover, maximum slip frequency $\omega_{sl\,\max}$ and maximum available force can be written as:

$$\omega_{sl\;max}\big(f(Q)\big) = \frac{R_r'}{L'_{lr}+L_m(1-f(Q))}\,\frac{i^*_{qs\,lim}(f(Q))}{i^*_{ds}(f(Q))}, \tag{21}$$

$$F_{max} = \frac{n}{2}\,\frac{\pi}{\tau}\,\frac{{L_m}^2}{L'_r}\; i^*_{qs\,lim} i^*_{ds}. \tag{22}$$

By increasing the LIM speed, the voltage limit ellipse decreases. The constant force area ends when the nominal *d*-axis current, i_{ds_rated}, coincides with the crossing point of the ellipse and the circle (as shown in Figure 4). This point is related to the base frequency, ω_b.

5.2. Partial FW area ($\omega_b < \omega_e < \omega_c$)

The partial FW area is the region between the base frequency and the critical frequency, ω_c [12]. In this area, the reference *d*-axis current, i^*_{ds}, can be computed as [21]:

$$i^*_{ds} = \sqrt{\frac{-2AC + B^2 I^2_{\max} - B\sqrt{-4ACI^2_{\max} + I^4_{\max}B^2 - 4C^2}}{2(A^2+B^2)}}. \tag{23}$$

The maximum command *q*-axis current, $i^*_{qs\,lim}$, can be written as [21]:

$$i^*_{qs\,\mathrm{lim}} = \sqrt{\frac{-2DF + E^2 I^2_{\max} + E\sqrt{-4FDI^2_{\max} + I^4_{\max}E^2 - 4F^2}}{2(D^2+E^2)}}, \tag{24}$$

where:

$$A = (L^2_\sigma . L^2_s - L^4_\sigma).\omega^4_e + (L^2_s - L^2_\sigma).R^2_s.\omega^2_e, \tag{25}$$

$$B = 2(L^2_\sigma . L_s - L^3_\sigma).R_s.\omega^3_e + 2(L_s - L_\sigma).R^3_s.\omega_e \tag{26}$$

$$C = -(R^2_s + L^2_\sigma .\omega^2_e).V^2_{max} + (R^2_s + L^2_\sigma .\omega^2_e)^2.I^2_{max} \tag{27}$$

$$D = (L^2_\sigma . L^2_s - L^4_\sigma).\omega^4_e - (L^2_s - L^2_\sigma).R^2_s.\omega^2_e \tag{28}$$

$$E = 2(L^3_s - L_\sigma L^2_s).R_s.\omega^3_e + 2(L_s - L_\sigma).R^3_s.\omega_e \tag{29}$$

$$F = -(R^2_s + L^2_s.\omega^2_e).V^2_{max} + (R^2_s + L^2_s.\omega^2_e)^2.I^2_{max} \tag{30}$$

Substituting Eqs. (23) and (24) into Eqs. (21) and (22), the maximum slip frequency and maximum available force can be calculated, respectively.

As shown in Figure 5, in the partial FW area, the rated *d*-axis current i_{ds_rated} is always greater than the reference *d*-axis current.

The critical speed, ω_c, is the speed above which no crossing point exists between the voltage constraint ellipse and the current constraint circle (as represented in Figure 6).

5.3. Full FW area ($\omega_e \geq \omega_c$)

The area above the critical speed, ω_c, is called the full FW region (as shown in Figure 7).

In the full FW area, the command *d*-axis current, , i^*_{ds}, can, can be computed as [21]:

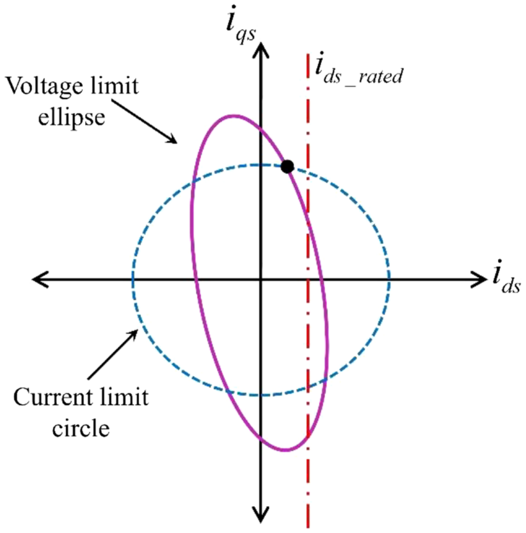

Figure 5. Partial FW area (FW-I).

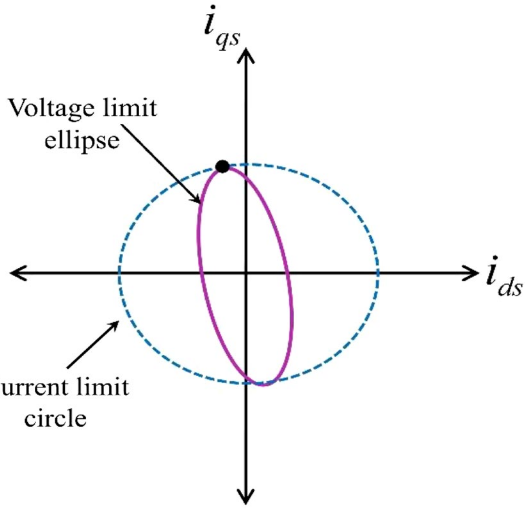

Figure 6. Determination of the critical speed.

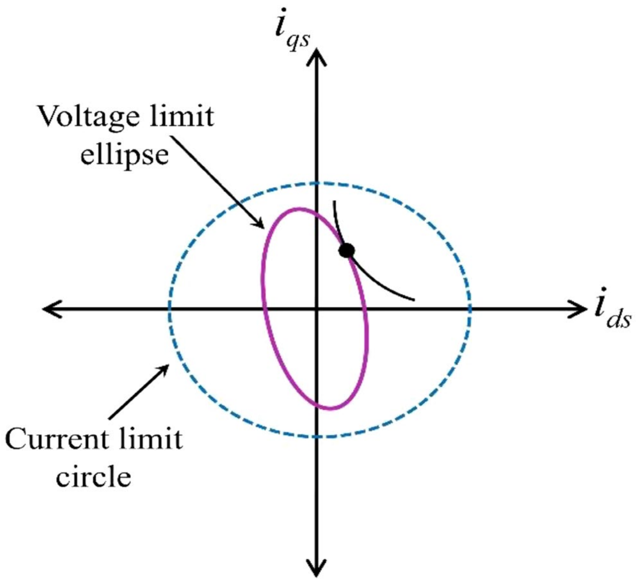

Figure 7. Full FW area (FW-II).

$$i_{ds}^{*}=\sqrt{\frac{-4A_2C_2+B_2C_2\left(B_2+\sqrt{B_2^2-4A_2}\right)}{2\left(4A_2^2-A_2B_2^2\right)}}. \tag{31}$$

The maximum command q-axis current, $i_{qs_{lim}}^{*}$, can be written as [21]:

$$i_{qs_{lim}}^{*}=\sqrt{\frac{-4A_2C_3+B_2C_3\left(B_2+\sqrt{B_2^2-4A_2}\right)}{2(4A_2^2-A_2B_2^2)}}, \tag{32}$$

where

$$A_2=-(R_s^2+L_\sigma.L_s.\omega_e^2)^2, \tag{33}$$
$$B_2=2(L_\sigma-L_s)\omega_e.R_s\ , \tag{34}$$
$$C_2=(R_s^2+L_\sigma^2.\omega_e^2).V_{max}^2\ , \tag{35}$$
$$C_3=(R_s^2+L_s^2.\omega_e^2).V_{max}^2\ . \tag{36}$$

Substituting Eqs. (31) and (32) into Eqs. (21) and (22), the maximum slip frequency and maximum available force can be calculated, respectively.

6. Control system

Figure 8 represents the overall field-weakening IFOC diagram for a three-phase LIM drive. The control diagram contains an outer speed controller and an inner current controller. This work uses the FLC in the speed control loop to produce the command q-axis current (i_{qs}^{*}). The speed regulator obliges the LIM to follow the command speed. The FW block generates the reference d-axis current (i_{ds}^{*}), the maximum q-axis current (i_{qslim}^{*}), and the maximum slip frequency ($\omega_{sl\,max}$). Figure 9 shows the flowchart of the field-weakening block. The reference three-phase currents are generated utilizing the inverse Park's transformation. These currents are then used in the current controller loop. By comparing the reference and actual currents in a hysteresis modulation block, the switching pulses of the inverter are generated.

Table 1: FLC rule base matrix.

	ΔV_n				
Δe_n	**NH**	**NL**	**ZE**	**PL**	**PH**
NE	NH	NL	NC	PM	PH
ZE	NH	NL	NC	PM	PH
PO	NH	NL	PL	PM	PH

7. FLC strategy

According to the LIM model, the present sample of speed error $\Delta V_r(n)$ and the change of speed error $\Delta e(n)$ are considered as the input variables of the FLC [34,35]. The reference LIM thrust ($F_e^{*}(n)$) is chosen as the output variable of the FLC [34]. After calculating $F_e^{*}(n)$, the reference q-axis primary current (i_{qs}^{*}) can be computed using Eq. (22). n is the present sample. Figure 10 represents the IFOC diagram of the LIM drive based on the FLC with FW control. The factors K_ω and K_e normalize $\Delta V_r(n)$ and $\Delta e(n)$ within the limit ± 1, respectively. K_i must be appropriately chosen to produce the accurate command thrust. These gains are tuned by trial and error to get perfect simulation results of the LIM drive. The fuzzy rules used in the FLC are as follows [34]:

- If ΔV_n is PH (Positive High), then F_e^{*} is PH;
- If ΔV_n is PL (Positive Low), then $F_e^{*}$is PM (Positive Medium);
- If ΔV_n is ZE (Zero) and Δe is PO (Positive), then F_e^{*} is PL;
- If ΔV_n is ZE and Δe is NE (Negative), then F_e^{*} is NC (No Change);
- If ΔV_n is ZE and Δe is ZE, then F_e^{*} is NC;
- If ΔV_n is NL (Negative Low), then F_e^{*} is NL;
- If ΔV_n is NH (Negative High), then F_e^{*} is NH.

Figure 11 shows the membership functions for fuzzy sets [34]. Table 1 represents the FLC rule base matrix. Mamdani-type fuzzy inference and the center of gravity method for defuzzification have been applied in this work.

8. Simulation results

To evaluate the correctness of the suggested LIM drive in the FW region, some simulation results are provided in this part. Simulation parameters are given in Appendix A.

The impact of the primary resistance and the end effect is initially studied in the FW control areas of LIM drive. Figure 12 shows the command d-axis current (i_{ds}^{*}) for three different operating speed regions using Eqs. (19), (23), and (31).

According to Figure 12, i_{ds}^{*} equations are dependent on the end effect through LIM speed and are also dependent on the synchronous frequency through loading conditions.

The base frequency is in accordance with the cross point of constant force area and partial FW area. The critical frequency is the cross point of partial FW area and full FW area. Figures 13 and 14 show the variations of the base and the critical frequencies with end effect, respectively. Results clearly show that when the end effect is considered, the base and the critical frequencies are not constant. This is due to the variation of the magnetizing inductance in the equivalent circuit model. Moreover, as the LIM speed increases, the base frequency reduces, whereas the critical frequency increases.

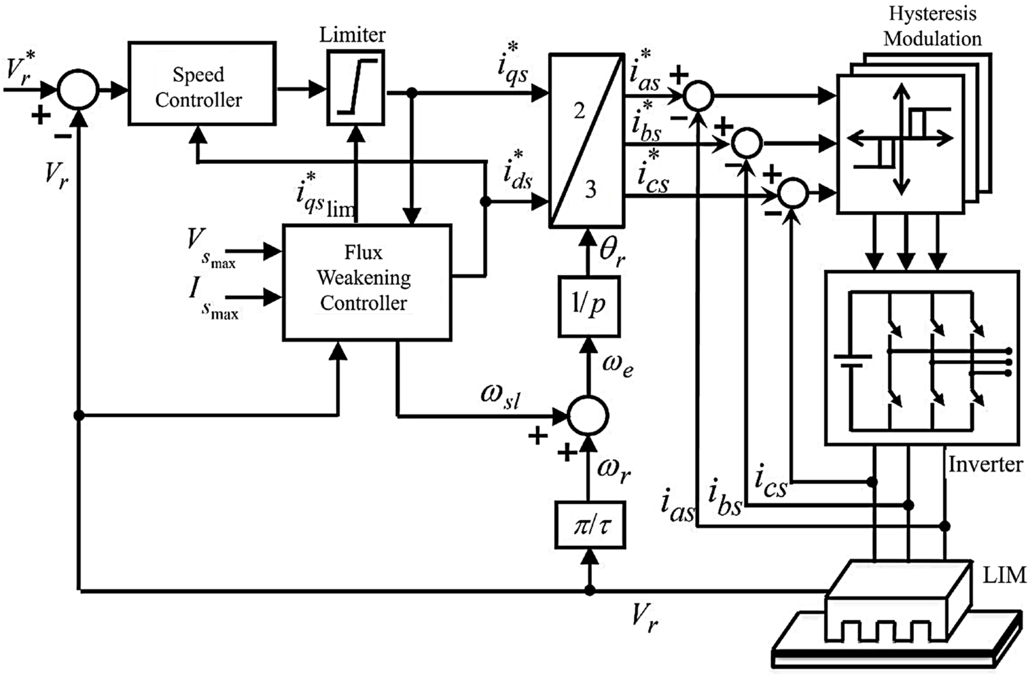

Figure 8. Overall block diagram of the FW IFOC for LIM drive.

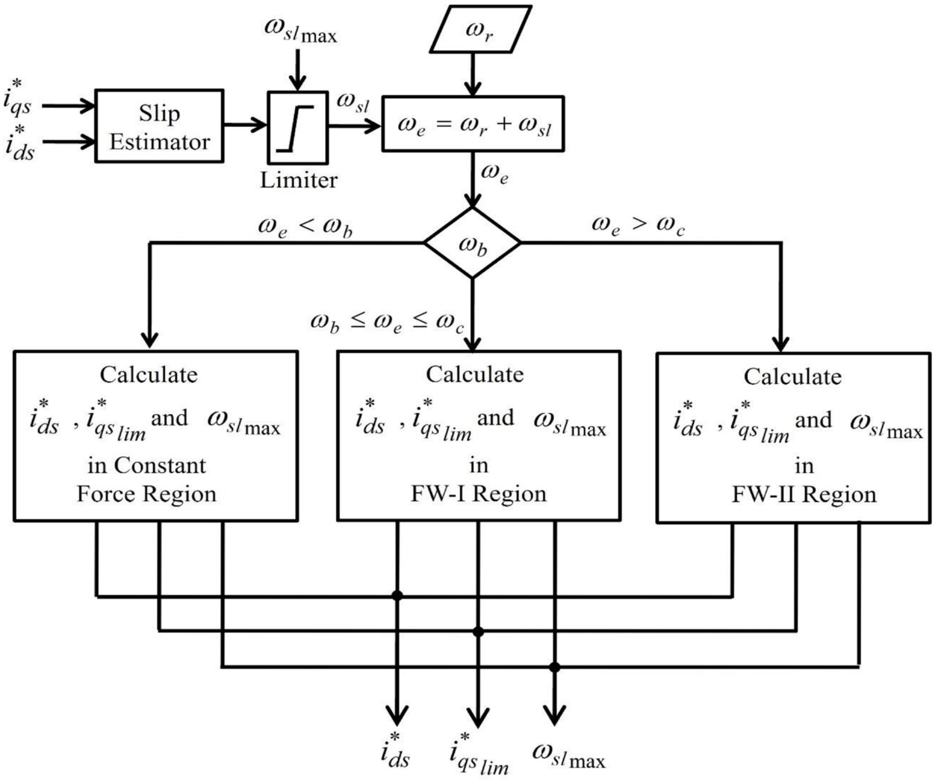

Figure 9. Flowchart of the FW block.

The maximum achievable LIM force along with the speed is illustrated in Figure A.1 in the Appendix A.

To implement the FW control of LIM drive in different operating speed areas, the reference control pattern must be extracted using Eqs. (19)-(36), considering the primary resistance and end effect. Figure 15 shows the reference *d* axis current (i_{ds}^*), maximum *q*-axis current ($i_{qs_{lim}}^*$), maximum slip frequency ($\omega_{sl\_\max}$), and maximum force, $F_{L\_\max}$ along with the angular frequency and $f(Q)$.

Using the extracted reference control pattern shown in Figure 15, the FW control of LIM drive has been carried out in different operating regions.

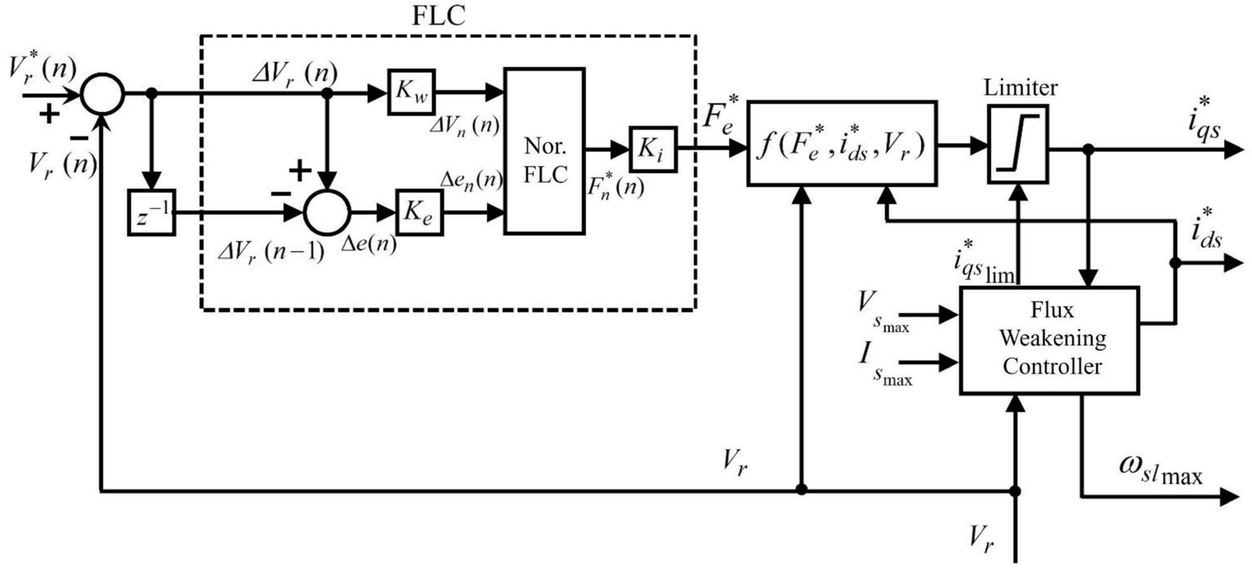

Figure 10. Block diagram of the FLC-based IFOC of LIM drive with the FW control.

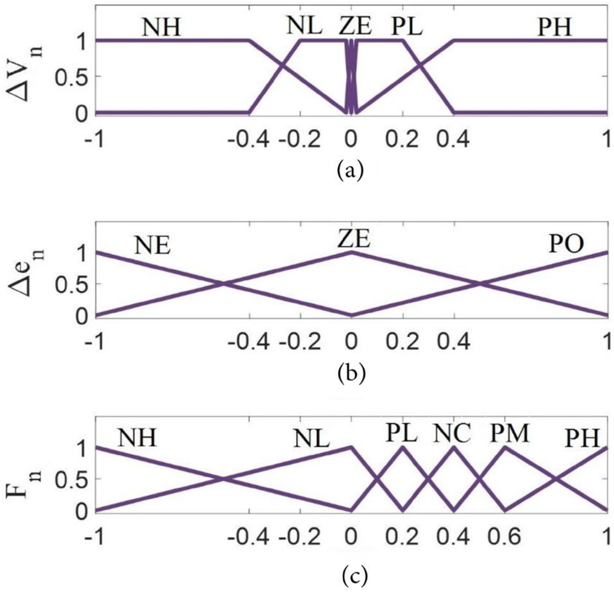

Figure 11. FLC membership functions; (a) Speed error ΔV_n; (b) Speed error change Δe_n; (c) Thrust $F_n^*(n)$.

Figure 16(a) illustrates the reference and actual LIM speed. The initial speed reference is considered equal to 20 m/sec and is than increased to 35 m/sec in *t=4* sec. The speed reference is reduced to 15 m/sec in *t=7* sec. External load changes are applied to the LIM drive in *t=2, 3, 6*, and 9 sec. The LIM speed clearly tracks the reference in different operating conditions with no overshoot.

Figure16(b) and (c) show the LIM phase current and phase voltage in different operating conditions. The LIM current and voltage are limited to their maximum allowable values, i.e., $I_{s\_\max}$ and $V_{s\_\max}$, respectively. The results manifest the accuracy of the LIM drive with the field-weakening control strategy. Figure 16(d) and (e) show the current constraint curve ($i_{ds}^2+i_{qs}^2$) and the voltage constraint curve ($v_{ds}^2+v_{qs}^2$), respectively. The current and voltage constraints are regarded in different operating conditions. Thus, the LIM current and voltage waveforms are restricted to their maximum allowable values. The areas in which the current constraint is limited to $I_{s\_\max}$ is related to the partial FW area. The areas limited to $V_{s\_\max}$ due to the voltage constraint are in accordance with the full FW area.

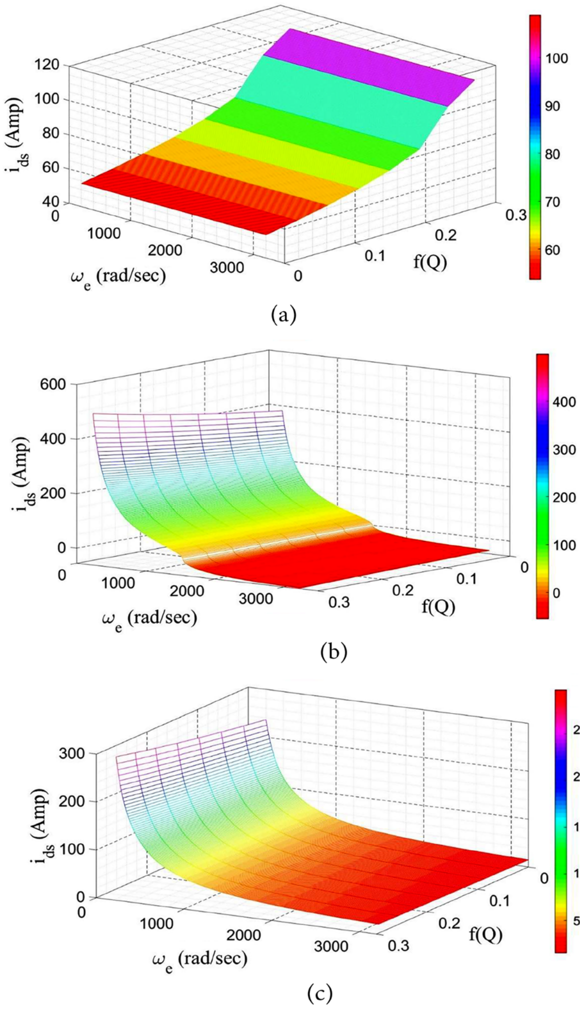

Figure 12. Command *d*-axis current along with the frequency with end effect: (a) Constant force area; (b) Partial FW area; and (c) Full FW area.

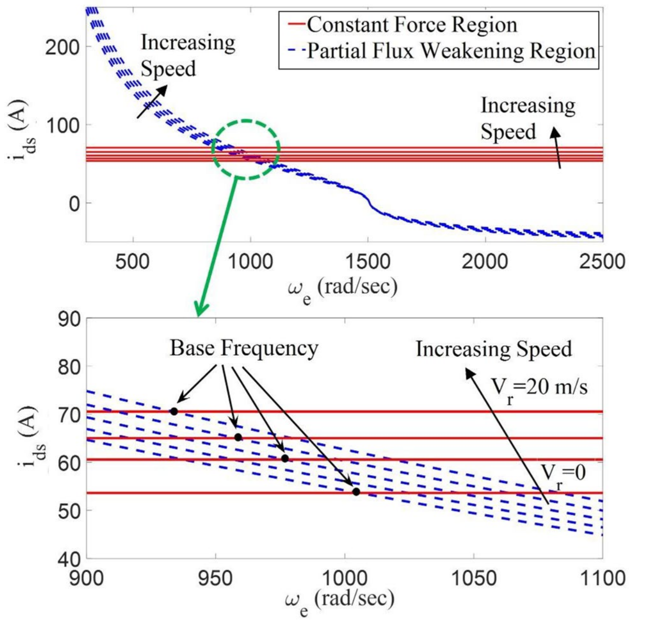

Figure 13. Variation of base angular frequency, ω_b, with end effect.

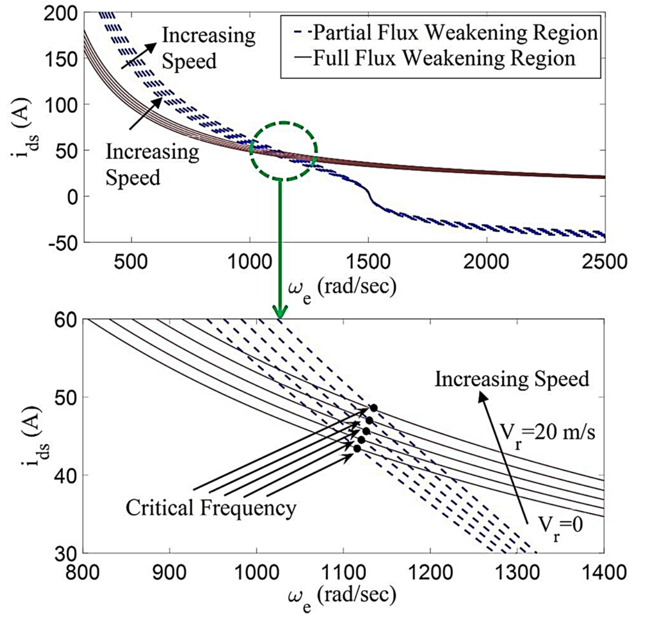

Figure 14. Variation of critical angular frequency, ω_c, with end effect.

In Figure 16(f), the angular frequency of the LIM drive is represented and compared with base frequency ω_b and the critical frequency ω_c. The regions above the critical frequency are relevant to the full FW area. The areas between the base and the critical frequencies are in accordance with the partial FW area. Below the base frequency is the constant force region.

It is clear from the results that the proposed FW control of the LIM drive based on FLC offers satisfactory speed tracking performance under various loading conditions and different operating speed regions.

9. Conclusion

This work provides a novel Flux-Weakening (FW) control pattern for the Linear Induction Motor (LIM) drive considering the end effect and primary resistance. In this scheme, the reference *d*-axis current and the reference maximum *q*-axis current are extracted in three operational speed regions regarding the end effect and the primary resistance. The base and the critical speeds are automatically calculated during the algorithm from the crossing points of the reference *d*-axis currents in different operating areas. Furthermore, the Fuzzy Logic Controller (FLC) has been successfully implemented to overcome the nonlinear behavior of the LIM drive with FW strategy and to improve the dynamic characteristics. Simulation results manifest that the suggested FLC-based LIM drive with FW control method has good tracking performance in various operating speed areas while the voltage and current constraints are

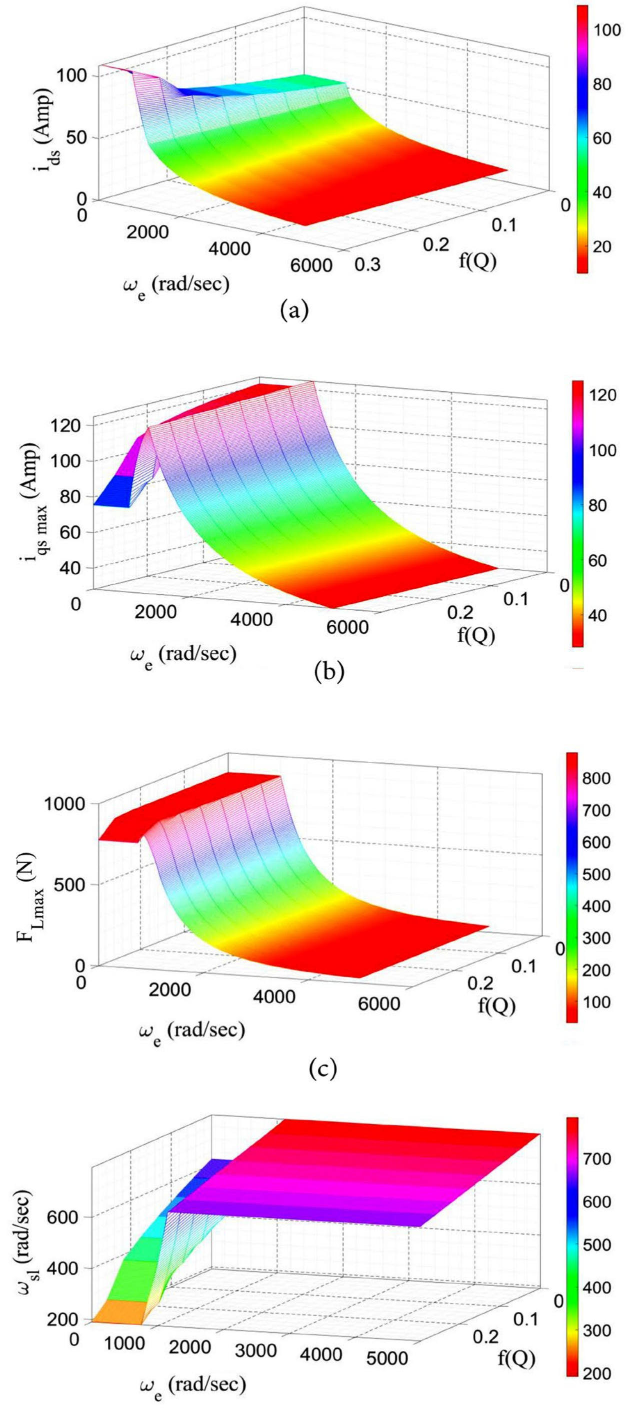

(a)

(b)

(c)

(d)

Figure 15. FW reference control pattern: (a) *d*-axis current, (b) Maximum q-axis current, (c) Maximum slip frequency, and (d) Maximum force capability along with the speed with end effect.

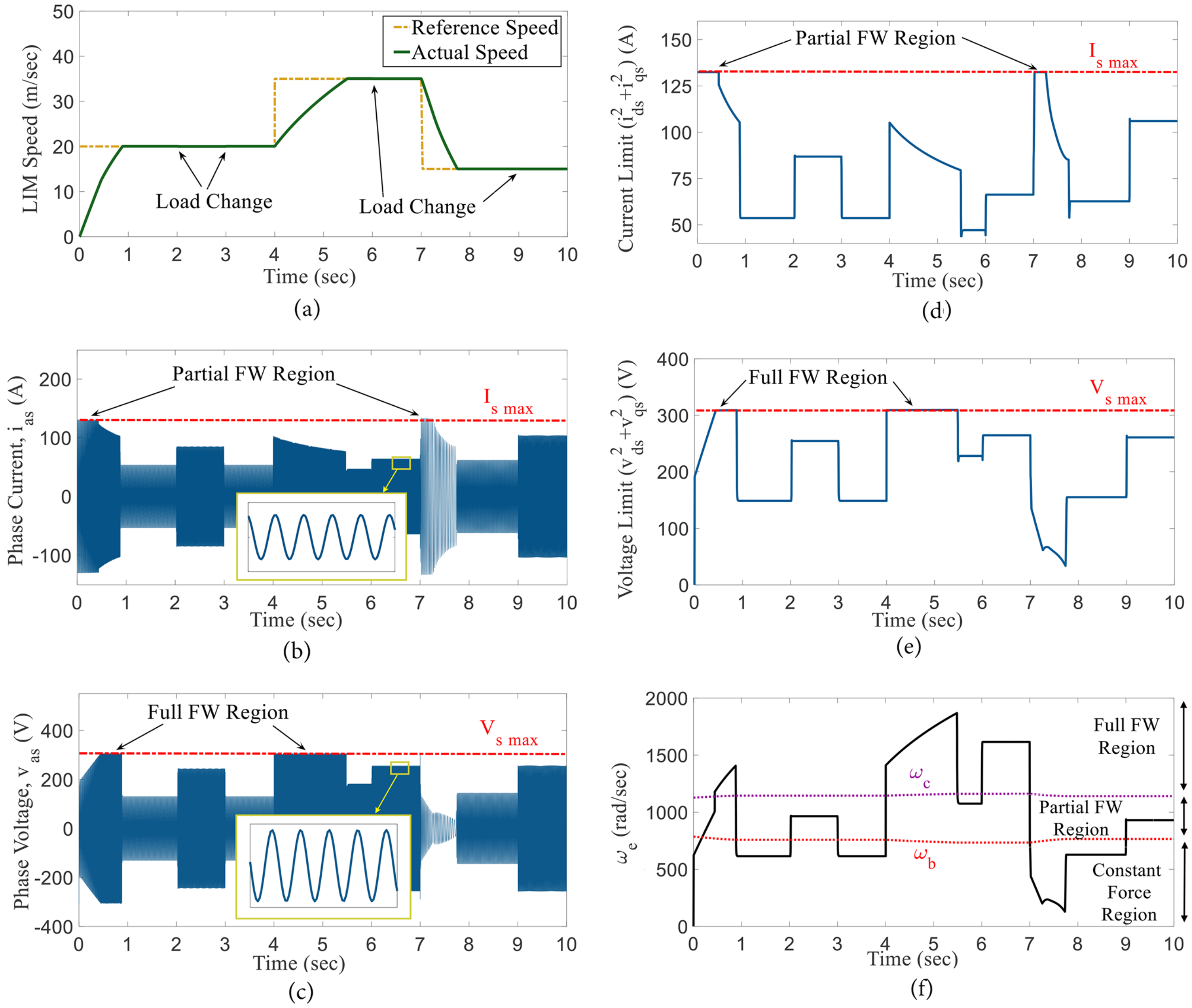

(a) (d) (b) (e) (c) (f)

Figure 16. FW control of LIM drive: (a) Speed response, (b) Phase current, (c) Phase voltage, (d) Current constraint, (e) Voltage constraint, and (f) Angular frequency with end effect.

satisfied. The speed response tracks the reference fast with no overshoot and low steady-state error in various loading conditions. It is shown that in a LIM drive with end effect consideration, the base and the critical speed are not constant due to the variation in the magnetizing inductance. According to the results, when the primary resistance and end effect are considered, increasing the LIM synchronous frequency will reduce the base frequency and increase the critical frequency.

Funding

This research did not receive any specific grant from funding agencies in the public, commercial, or not-for-profit sectors.

Conflicts of interest

The author declares that they have no known competing financial interests or personal relationships that could have appeared to influence the work reported in this paper.

Author contribution statement

Pegah Hamedani Conceptualization; Data curation; Formal analysis; Investigation; Methodology; Project administration; Resources; Software; Supervision; Validation; Visualization; Roles/Writing – original draft; Writing – review and editing.

References

1. Wang, K., Li, Y., Ge, Q., et al. "An improved indirect field-oriented control scheme for linear induction motor traction drives," *IEEE Transactions on Industrial Electronics*, **65**(12), pp. 9928-9937 (2018). DOI: 10.1109/TIE.2018.2815940
2. Sul, S.K., *Control of Electric Machine Drive Systems*, Wiley-IEEE Press (2011). DOI:10.1002/9780470876541
3. Quang, N.P. and Dittrich, J.A., *Vector Control of Three-Phase AC Machines: System Development in the Practice"*, Springer (2015). DOI: 10.1007/978-3-662-46915-6
4. Rodriguez, J. and Cortes, P., *Predictive Control of Power Converters and Electrical Drives,* John Wiley & Sons (2012). DOI: 10.1002/9781119941446
5. Accetta, A., Cirrincione, M., Pucci, M., et al. "State space-vector model of linear induction motors including end-effects and iron losses Part I: Theoretical analysis,"

IEEE Transactions on Industry Applications, **56**(1), pp. 235-244 (2020). DOI: 10.1109/TIA.2019.2952031

6. Hu, D., Xu, W., Dian, R., et al. "Loss minimization control of linear induction motor drive for linear metros", *IEEE Transactions on Industrial Electronics*, **65**(9), pp. 6870-6880 (2018). DOI: 10.1109/TIE.2017.2784343
7. Susluoglu, B. and Karsli, V.M. "Direct thrust controlled linear induction motor including end effect", In *Proc. of the 13th International Power Electronics and Motion Control Conference (EPE-PEMC)*, pp. 850-854 (2008). DOI: 10.1109/EPEPEMC.2008.4635373
8. Zhao, J., Yang, Z., Liu, J., et al. "Indirect vector control scheme for linear induction motors using single neuron PI controllers with and without the end effects", In *Proc. of the 7th Word Congress on Intelligent Control and Automation*, China, pp. 5263-5267 (2008). DOI: 10.1109/WCICA.2008.4593785
9. Sung, J.H. and Nam, K. "A new approach to vector control for a linear induction motor considering end effects", In *Proc. of the IEEE Industry Applications Conference,* **4**, pp. 2284-2289 (1999). DOI: 10.1109/IAS.1999.799162.
10. Silva, E.F., Santos, E.B., Machado, P.C.M., et al. "Vector control for linear induction motor", In *3rd IEEE International Conference on Industrial Technology (ICIT 2003)*, Maribor, Slovenia, pp. 518-523 (2003). DOI: 10.1109/ICIT.2003.1290384
11. Duncan, J. "Linear induction motor-equivalent-circuit model", *IEE Proc. Power Application*, **130**(1), pp. 51-57 (1983). DOI: 10.1049/ip-b.1983.0008
12. Kang, G. and Nam, K. "Field-oriented control scheme for linear induction motor with the end effect", *IEE Proc. on Electric Power Appl.*, **152**(1), pp. 1565-1572 (2005). DOI: 10.1049/ip-epa:20045200 (https://digital-library.theiet.org/doi/10.1049/ip-epa%3A20045185)
13. Kim, S.H. and Sul, S.K. "Maximum torque control of an induction machine in the field weakening region", *IEEE Transactions on Industry Applications*, **31**(4), pp. 787-794 (1995). DOI: 10.1109/28.395288
14. Kim, S.H. and Sul, S.K. "Voltage control strategy for maximum torque operation of an induction machine in the field-weakening region", *IEEE Transaction on Industrial Electronics*, **44**(4), pp. 512-518 (1997). DOI: 10.1109/41.605628
15. Levi, E. and Wang, M. "A speed estimator for high performance sensor less control of induction motors in the field weakening region", *IEEE Transaction on Power Electronics*, **17**(3), pp. 365-378 (2002). DOI: 10.1109/TPEL.2002.1004244
16. Seok, J.K. and Sul, S.K. "Optimal flux selection of an induction machine for maximum torque operation in flux-weakening region", *IEEE Transaction on Power Electronics*, **14**(4), pp. 700-708 (1999). DOI: 10.1109/63.774208
17. Song, S.H. Choi, J.W., and Sul, S.K. "Transient torque maximizing strategy of induction machine in field weakening region", *In IEEE Power Electronics Specialists Conference* (PESC), **2**, Fukuoka, pp. 1569-1574 (1998). DOI: 10.1109/PESC.1998.703387
18. Nguyen-Thac, K., Orlowska-Kowalska, T., and Tarchala, G. "Comparative analysis of the chosen field-weakening methods for the direct rotor flux oriented control drive system", *Archives of Electrical Engineering*, **61**(4), pp. 443-454 (2012). DOI: 10.2478/v10171-012-0038-7
19. Nguyen-Thac, K., Orlowska-Kowalska, T., and Tarchala, G. "Influence of the stator winding resistance on the field-weakening operation of the DRFOC induction motor drive", *Bulletin of the Polish Academy of Sciences –Technical Sciences*, **60**(4), pp. 815-823 (2012). DOI: 10.2478/v10175-012-0095-5
20. Bianchi, N., Carlet, P.G., Cinti, L., et al. "Review about flux-weakening operating limits and control techniques for synchronous motor drives", *Energies*, **15**(5), p. 1930 (2022). DOI: 10.3390/en15051930
21. Lopez, G.G., Gunawan, F.S., and Walters, J.E. "Current control of induction machines in the field-weakened region", *IEEE Transactions on Industry Applications*, **43**(4), pp. 981-989 (2007). DOI: 10.1109/TIA.2007.900459
22. Wu, C., Yang, J., and Li, Q. "GPIO-Based nonlinear predictive control for flux-weakening current control of the IPMSM servo system", *Energies*, **13**(7), pp. 1-21 (2020). DOI: 10.3390/en13071716
23. Liu, J., Gong, C., Han, Z., et al. "IPMSM model predictive control in flux-weakening operation using an improved algorithm", *IEEE Transactions on Industrial Electronics*, **65**(12), pp. 9378-9387 (2018). DOI: 10.1109/TIE.2018.2818640
24. Zhang, Y., Jin, J., Jiang, H., et al. "Adaptive PI parameter of flux-weakening controller based on voltage feedback for model predictive control of SPMSM", *2020 IEEE Energy Conversion Congress and Exposition (ECCE*), Detroit, USA, pp. 2674-2681 (2020). DOI: 10.1109/ECCE44975.2020.9235453
25. Hou, P., Wang, X., and Sheng, Y. "Research on flux-weakening control system of interior permanent magnet synchronous motor based on fuzzy sliding mode control", In *2019 Chinese Control and Decision Conference (CCDC)*, Nanchang, China, pp. 3151-3156 (2019). DOI: 10.1109/CCDC.2019.8832483
26. Xu, W., Ismail, M.M., Liu, Y., et al. "Parameter optimization of adaptive flux-weakening strategy for permanent-magnet synchronous motor drives based on particle swarm algorithm", *IEEE Transactions on Power Electronics*, **34**(12), pp. 12128-12140 (2019). DOI: 10.1109/TPEL.2019.2908380
27. Wang, C. and Zhu, Z.Q. "Fuzzy logic speed control of permanent magnet synchronous machine and feedback voltage ripple reduction in flux-weakening operation region", *IEEE Transactions on Industry Applications*, **56**(2), pp. 1505-1517 (2020). DOI: 10.1109/TIA.2020.2967673
28. Xu, Y., Morito, Ch., and Lorenz, R.D. "Extending high-speed operating range of induction machine drives using deadbeat-direct torque and flux control with precise flux weakening", *IEEE Transactions on Industry Applications*, **55**(4), pp. 3770-3780 (2019). DOI: 10.1109/TIA.2019.2908342

29. Cai, H., Xu, L., and Pina, A.J. “Maximum torque control of induction machine in deep flux weakening region”, *In 2015 IEEE Energy Conversion Congress and Exposition (ECCE)*, Montreal, Canada, pp. 20-24 (2015). DOI: 10.1109/ECCE.2015.7310215
30. Dong, Zh., Yu, Y., Li, W., et al. “Flux-weakening control for induction motor in voltage extension region: Torque analysis and dynamic performance improvement”, *IEEE Transactions on Industrial Electronics*, **65**(5), pp. 3740–3751 (2018). DOI: 10.1109/TIE.2017.2764853
31. Dong, Zh., Wang, B., Yu, Y., et al. “Operating point selected flux-weakening control of induction motor for torque-improved high-speed operation under multiple working conditions”, *IEEE Transactions on Power Electronics*, **34**(12), pp. 12011-12023 (2019). DOI: 10.1109/TPEL.2019.2905536
32. Xu, W., Tang, Y., Dong, D., et al. “Optimal reference primary flux based model predictive control of linear induction machine with MTPA and field-weakening operations for urban transit”, *IEEE Transactions on Industry Applications*, **58**(4), pp. 4708-4721 (2022). DOI: 10.1109/TIA.2022.3166458
33. Zou, J., Xu, W., Yu, X., et al. “Multistep model predictive control with current and voltage constraints for linear induction machine based urban transportation”, *IEEE Transactions on Vehicular Technology*, **66**(12), pp. 10817-10829 (2017). DOI: 10.1109/TVT.2017.2736533
34. Hamedani, P. and Shoulaie, A. “Modification of the field-weakening control strategy for linear induction motor drives considering the end effect”, *Advances in Electrical and Computer Engineering (AECE)*, **15**(3), pp. 3-12 (2015). DOI: 10.4316/AECE.2015.03001
35. Hamedani, P., Sadr, S., and Shoulaie, A. “Independent fuzzy logic control of two five-phase linear induction motors supplied from a single voltage source inverter”, *Journal of Electrical and Computer Engineering Innovations (JECEI)*, **10**(1), pp. 195-208 (2021). DOI: 10.22061/JECEI.2021.8091.479
36. Hamedani, P. and Shoulaie, A. “Utilization of CHB multilevel inverter for harmonic reduction in fuzzy logic controlled multiphase LIM drives”, *Journal of Electrical and Computer Engineering Innovations (JECEI)*, **8**(1), pp. 19-30 (2020). DOI: 10.22061/JECEI.2020.6664.355

Appendix

FLC gains: K_ω=0.0257, K_e=1.5, K_i=1813.

The LIM parameters are given in Table A.1. Figure A.1 shows the force-speed characteristics with end effects.

Table A.1: LIM parameters.

Parameter	Value
Phase voltage	220 V
Current	93.65 A
Power factor	0.4884
Pole pairs	2
Pole pitch	0.1024 m
LIM length	0.413 m
R_s	0.049 Ω
R'_r	0.803 Ω
L_{ls}	1.5 mH
L'_{lr}	4% L_{ls}
L_m	3 mH
λ^*_{dr}	0.24 Wb
M	29.34 kg
Slip	0.5
Rated force	879 N

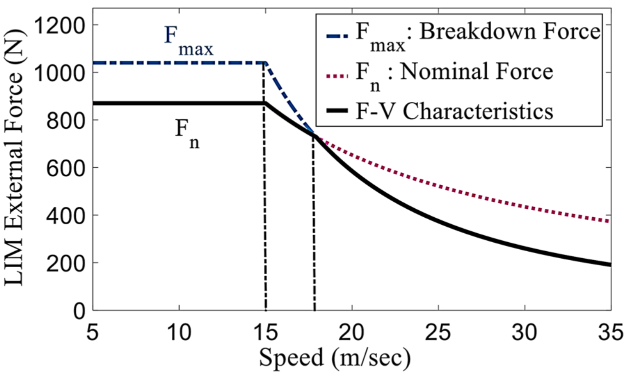

Figure A.1. Force-speed characteristics with end effect.

Biography

Pegah Hamedani was born in Isfahan, Iran, in 1985. She received BSc and MSc degrees from University of Isfahan, Iran, in 2007 and 2009, respectively, and the PhD degree from Iran University of Science and Technology, Tehran, in 2016, all in Electrical Engineering. Her research interests include power electronics, control of electrical motor drives, supply system of the electric railway (AC and DC), linear motors & MAGLEVs, and analysis of overhead contact systems. She is currently an Assistant Professor with the Department of Railway Engineering and Transportation Planning, University of Isfahan, Isfahan, Iran. Dr. Hamedani was the recipient of the IEEE 11th Power Electronics, Drive Systems, and Technologies Conference (PEDSTC’20) best paper award in 2020.